Multiple toroidal dipole Fano resonances of asymmetric dielectric nanohole arrays

Chaobiao Zhou [1,2,3,*] Shiyu Li,[2,*] Yi Wang,[2,†] and Mingsheng Zhan[2,3,‡]

[1]*College of Mechanical and Electronic Engineering, Guizhou Minzu University, Guiyang 550025, China*

[2]*Wuhan National Laboratory for Optoelectronics, Huazhong University of Science and Technology, Wuhan 430074, China*

[3]*State Key Laboratory of Magnetic Resonance and Atomic and Molecular Physics, Wuhan Institute of Physics and Mathematics, Chinese Academy of Sciences, Wuhan 430071, China*

(Received 4 September 2019; revised manuscript received 4 November 2019; published 18 November 2019)

The toroidal dipole is a fundamental electromagnetic excitation independent from the well-known electric and magnetic dipoles, which enables strong resonances in nanostructure systems due to the reduction of radiative loss. In this paper, we demonstrate multiple toroidal dipole resonances in a series of silicon nanohole structures with symmetry breaking in the near-infrared range. Detailed multipole decompositions and field distributions are performed to discuss the excitation of these resonances. The following experimental verifications support the theoretical predictions. Such a two-dimensional nanohole platform could be more technically available compared to other complicated nanostructures. Our results may provide remarkable potentials in facilitating the light-matter interaction at the nanoscale, such as light emission, subtle sensing, and so on.

DOI: 10.1103/PhysRevB.100.195306

I. INTRODUCTION

Optical resonances supported by subwavelength nanostructures are extremely important for various applications in nanophotonics including light emission [1–5], sensing [6–8], optical switching [9,10], harmonic generation [11–16], etc., due to their sharp spectrum features and large local electromagnetic fields. Major elementary electromagnetic sources contributed to optical resonances include the electric dipole, magnetic dipole, and toroidal dipole. An electric dipole stems from a separation of positive and negative charges, whereas a magnetic dipole is created by the closed loop of an electric current, which are both familiar dipole patterns with wide applications. The toroidal dipole, a third independent family of elementary electromagnetic sources, is produced by poloidal currents with a corresponding closed head-to-tail magnetic loop, which was first introduced in 1957 by Zel'dovich in systems of nuclear physics [17]. The toroidal dipole response in natural media is typically very weak and hardly measurable since it arises against the background of much stronger electric and magnetic multipoles, thus, it has always been overlooked [18]. Recently, toroidal electrodynamics have been extensively studied, after Zheludev *et al.* experimentally demonstrated toroidal dipole resonances in an array of metal nanostructures at the microwave regime in 2010 [19]. The strong toroidal dipole resonances have been used as a platform for applications in ultrasensitive sensors [20,21], optical modulators [22,23], and so on. In particular, an extremely important function for toroidal dipole resonance is to assist in the achievement of an anapole mode, a nonradiating charge-current configuration [24–30]. At present, toroidal dipole resonances are mainly achieved in a variety of plasmonic structures made of metals [19–21,23,31–36]. However, these plasmonics suffer from high losses of metals and heating [37].

Recently, all-dielectric materials with a high refractive index have emerged as the essential building blocks for various functional resonators, due to their low dissipative losses, compatibility with semiconductor fabrication, and capabilities to trap the optical modes within dielectric nanostructures compared with their metallic counterparts [38–48]. In 2015, Basharin *et al.* theoretically pushed toroidal resonance to all-dielectric nanostructure media in the THz region of the spectrum, which exhibits significantly lower loss compared to metallic nanostructures [49]. Not long ago, Sayanskiy *et al.* theoretically studied the toroidal dipole response of all-dielectric metalattices in the visible region and made an experimental demonstration in the microwave frequency range [50]. Xu *et al.* experimentally demonstrated the toroidal dipole modes in all-dielectric resonant metasurfaces based on trimers in the microwave frequency range [51], and Tuz *et al.* theoretically studied the toroidal response in all-dielectric disks with symmetry breaking in the near-infrared region [52]. Experimental verifications of toroidal dipole resonances are rare in the important near-infrared region.

In this paper, we experimentally demonstrate strong toroidal dipole resonances in a series of all-dielectric nanohole arrays in the near-infrared range. First, the symmetry breaking is introduced through employing rectangular lattices for independent circular or square hole arrays to achieve multiple strong Fano resonances. Further, by performing Cartesian multipole decomposition, four of the six resonances and the other two are proved to be predominantly excited by the toroidal dipole and magnetic dipole, respectively. When another mirror symmetry along the y axis is broken by combining circular and square nanoholes within a lattice, the other three stronger resonances are excited, with one of

*These authors contributed equally to this work.

†ywangwnlo@mail.hust.edu.cn

‡mszhan@wipm.ac.cn

them predominantly contributed by a toroidal dipole and the other two predominantly contributed by a magnetic dipole. These results have been sufficiently verified by experimental performances.

II. CHARACTERISTICS OF RESONANCES IN THE INDEPENDENT CIRCULAR OR SQUARE NANOHOLE ARRAYS

Periodic dielectric nanohole structures with a high refractive index support Fano resonance due to the coupling of in-plane discrete guided modes and vertical continuum free-space radiation modes [53,54]. In arrays with square lattices ($P_x = P_y$) at the Γ point in the Brillouin zone, where the array is illuminated at normal incidence, there are six types of eigenmodes classified by their symmetries employing the irreducible representation of the C_{4v} point group. Two of these modes form a doubly degenerate pair which are 90° rotated versions of each other and can be excited under normal incidence. The other four modes are nondegenerate uncoupled modes, which cannot be excited under normal incidence due to the symmetry mismatch between the modes and the incident plane wave [53,55–57]. When symmetry mismatch is compensated via changing lattice parameters [57,58] or by imposing oblique incidences [13,55,56,59], the nondegenerate dark mode, uncoupled to external radiation and possessed of an infinite lifetime, is excited. It is because the perturbations of symmetry will introduce additional degrees of freedom in the Fourier amplitudes, thus reducing the infinite lifetime nondegenerate mode into a long-lived leaky resonance [59]. Herein, we want to excite the nondegenerate modes and achieve high Q-factor resonances in the near-infrared region employing nanohole arrays embedded in the silicon slab. First, a rectangular lattice ($P_x \neq P_y$) with a circular nanohole, shown in Fig. 1(a), is considered to break the two mirror symmetries with respect to the two diagonal axes and excite the nondegenerate modes. In the simulation, the finite-difference time-domain (FDTD) method is used to analyze the transmission spectra and the mode distributions in detail. The nondegenerate nature of these modes means that they will only couple to a single polarization when the symmetry is broken [56,57]. As shown in Figs. 1(b) and 1(c), the excited six modes are symbolized by I, II, . . . , VI, with four and two of them excited by the p and s polarizations, respectively. Specifically, the p waves have an electric field polarized along the x axis, and s waves have an electric field polarized along the y axis. It is noted that modes IV and VI are polarization independent, in other words, they can be regarded as one mode, which is doubly degenerate (detailed discussions are given below). When circular holes are replaced by square holes in the rectangular lattice arrays as shown in Fig. 1(d), the same six modes are excited as illustrated in Figs. 1(e) and 1(f) because they hold the same symmetry properties. The deviation of mode positions between the two cases is induced by a slight change of the effective refractive index due to the different spatial volumes of circular and square nanoholes. These resonant modes possesss rich properties, and are contributed by different dipole oscillations, including the toroidal dipole.

To study each moment and their contributions to far-field radiation for multiple Fano resonances of Fig. 1, we perform

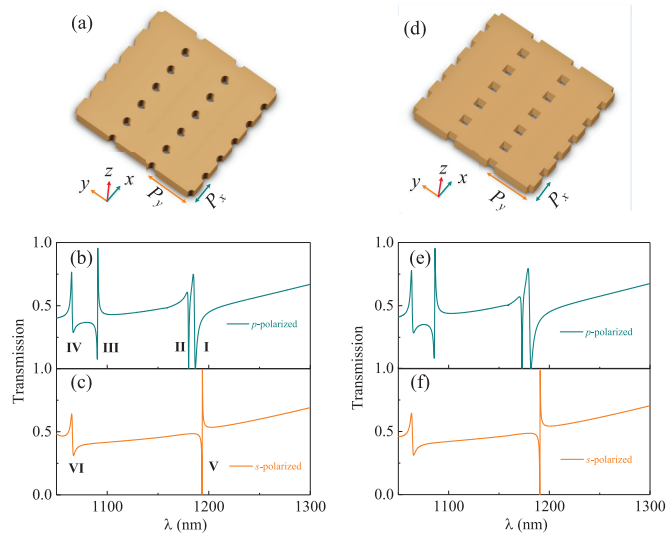

FIG. 1. Multiple resonances in silicon nanohole arrays. (a), (d) Schematic of nanohole arrays with $P_x = 400$ nm, $P_y = 800$ nm, $P_x \neq P_y$. The diameter of a circular hole is 120 nm, and the side length of a square nanohole is also 120 nm. The depth of the nanohole is 220 nm. (b), (c), (e), (f) Transmission spectra of the nanohole arrays for s-polarized and p-polarized light. Multiple sharp resonances are excited, which are labeled as I, II, . . . , VI.

a multipole decomposition under the Cartesian coordinate. According to the current density ($\vec{j}$) distribution in a unit cell with a circular hole of 120 nm diameter, which can be calculated through $\vec{j} = -i\omega\epsilon_0(n^2 - 1)\vec{E}$, all multipole moments can be defined as [28]

$$\vec{P} = \frac{1}{i\omega}\int \vec{j}d^3r, \tag{1}$$

$$\vec{M} = \frac{1}{2c}\int (\vec{r}\times\vec{j})d^3r, \tag{2}$$

$$\vec{T} = \frac{1}{10c}\int [(\vec{r}\cdot\vec{j})\vec{r} - 2r^2\vec{j}]d^3r, \tag{3}$$

$$Q^{(e)}_{\alpha\beta} = \frac{1}{2i\omega}\int \left[r_\alpha j_\beta + r_\beta j_\alpha - \frac{2}{3}(\vec{r}\cdot\vec{j})\delta_{\alpha,\beta}\right]d^3r, \tag{4}$$

$$Q^{(m)}_{\alpha\beta} = \frac{1}{3c}\int [(\vec{r}\times\vec{j})_\alpha r_\beta + [(\vec{r}\times\vec{j})_\beta r_\alpha]]d^3r, \tag{5}$$

where c and ω are the speed and angular frequency of light, respectively, and $\alpha, \beta = x, y, z$. The $\vec{P}$, $\vec{M}$, $\vec{T}$, $\vec{Q}^{(e)}$, $\vec{Q}^{(m)}$ are the electric dipole (ED) moment, magnetic dipole (MD) moment, toroidal dipole (TD) moment, electric quadrupole (EQ) moment, and magnetic quadrupole (MQ) moment, respectively. The scattered powers of these multipole moments are calculated from

$$I_P = \frac{2\omega^4}{3c^3}|\vec{P}|^2, \tag{6}$$

$$I_M = \frac{2\omega^4}{3c^3}|\vec{M}|^2, \tag{7}$$

$$I_T = \frac{2\omega^6}{3c^5}|\vec{T}|^2, \tag{8}$$

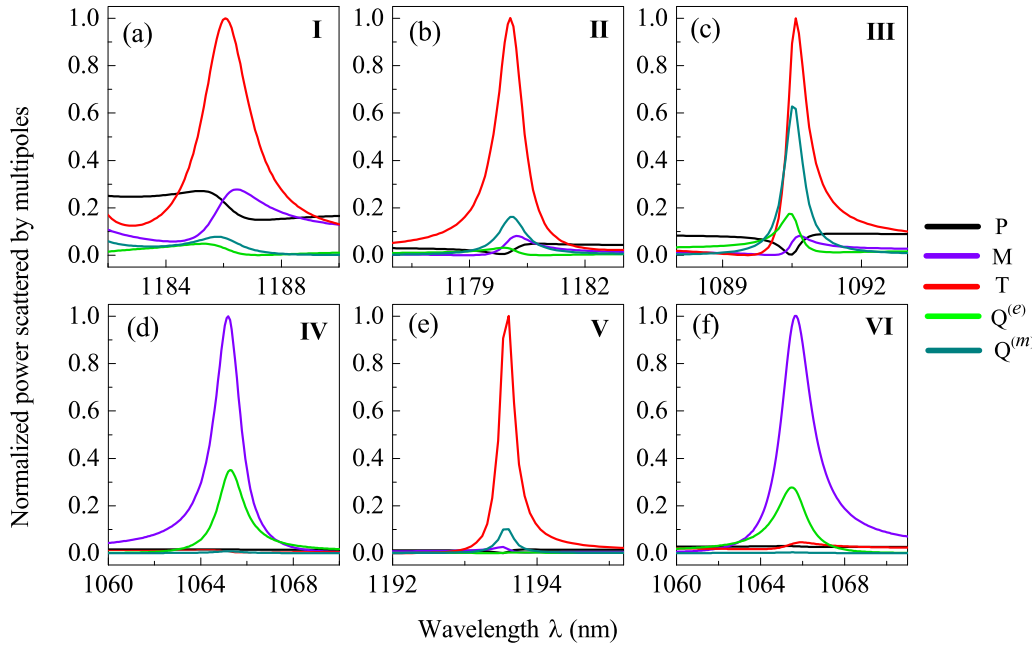

FIG. 2. Normalized scattering power of different multipole moments in circular nanohole arrays.

$$I_{Q^{(e)}} = \frac{\omega^6}{5c^5} \sum \left|\vec{Q}^{(e)}_{\alpha\beta}\right|^2, \tag{9}$$

$$I_{Q^{(m)}} = \frac{\omega^6}{40c^5} \sum \left|\vec{Q}^{(m)}_{\alpha\beta}\right|^2. \tag{10}$$

These decomposition results are shown in Fig. 2. It is clear that, for four of these modes which correspond to modes I, II, III, and V, the strongest contribution to the resonances is provided by the toroidal dipole moment, and the magnetic dipole moment contributes predominantly to the other modes IV and VI. As illustrated in Fig. 2(a), the toroidal dipole is the main contributor to mode I, and it is found that there also exist obvious contributions from other multipoles, especially electric and magnetic dipoles, which may interfere in the near field, resulting in a relatively broad resonance shown in Fig. 1(b). In general, there are often obvious magnetic quadrupole contributions accompanying the dominant toroidal dipole response, because both of them are induced by a pair of counteroriented magnetic dipoles [28,60], which are distinctly illustrated in modes II, III, V, and later mode VII. For modes II and V, the resonances are dominated by a combination of a magnetic quadrupole and a toroidal dipole, and the other multipoles are suppressed dramatically. As for mode III, besides the strongly excited toroidal dipole and magnetic quadrupole, the electric quadrupole makes an obvious contribution and the familiar electric and magnetic dipoles are suppressed greatly. As noted above, modes IV and VI correspond to a doubly degenerate pair, hence they support the same far-field radiation pattern. It can be demonstrated from Figs. 2(d) and 2(f) that the magnetic dipole contribution is predominant, and the electric quadrupole also serves as assistance.

In order to gain deeper insight into the physics of the multiple Fano resonances, we calculate the near-field distributions of modes I, II, …, VI, as shown in Fig. 3. The polarization-dependent mode excitation illustrated in Fig. 1 can be interpreted by considering the symmetry of each mode, which can be determined by the mode profile of the E_z component in the x-y plane [56]. The mode with a specific type of symmetry can only couple to the normally incident plane wave with the same type of symmetry [55–57]. From Figs. 3(a)–3(d), modes I, II, III, and IV are unchanged under the mirror reflection operation around the x axis and hence can only be excited by p-polarized light, owing to the same type of symmetry shared by the incident light and the modes. Similarly, modes V and VI are modified by a factor of -1 after the same reflection operation, indicating the excitation of these modes requires s-polarized incident light. In addition, it is noted that modes IV and VI are 90° rotated versions of each other, forming a doubly degenerate pair [57]. Then, the analysis of the field vector distributions serves as additional verification of the most contributive multipole components related to these six modes shown in Fig. 2. As for the electric field vector distributions of modes I, II, and III depicted in Figs. 3(a)–3(c), there are opposite circular electric fields generated in the x-y plane, giving rise to counteroriented magnetic components parallel along the z axis. Upon excitation with a p-polarized wave, a circular magnetic moment distribution perpendicular to the structure surface is generated, leading to a strong toroidal moment oriented along the x axis [see Figs. S1(a)–S1(c) and S2(a)–S2(c) [61]]. A similar process can also be found in mode V of Fig. 3(e) where the incident s-polarized light excites a toroidal dipole moment oriented along the y axis [see Figs. S1(e) and S2(e)]. Besides, it is noted that the opposite distribution of circular electric field possessed by mode I is not as obvious as the other three, which is attributed to the strong coupling of several dipoles in the near field. Specifically, the strong dipole moments, or relatively large scattering powers shown in Fig. 2(a), of the electric dipole and magnetic dipole in mode I, couple to the dominant toroidal dipole moment, resulting in the uncommon distribution pattern of the electric field. For mode III, the

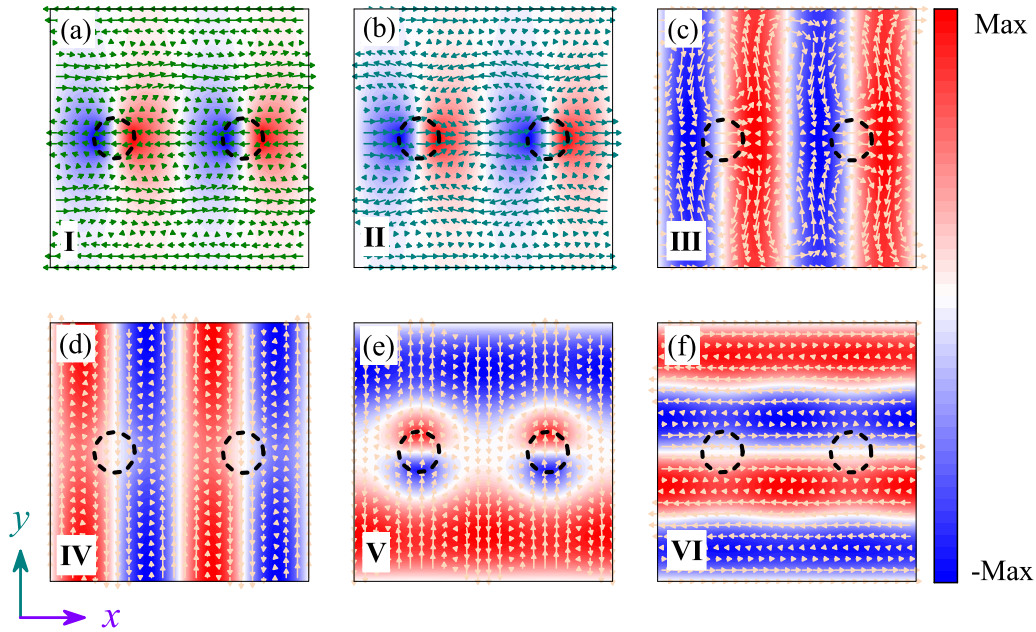

FIG. 3. Calculated electric field (z component E_z) distributions for six modes. Arrows show instantaneous directions of the electric (modes I, II, III, and V) and magnetic (modes IV and VI) field distribution.

magnetic quadrupole, which contributes much to the resonance, has little impact on the electric field pattern. That is because the generation of the magnetic quadrupole component in the y-z plane, which is the dominant component of it, requires pairs of counteroriented out-of-plane magnetic dipoles just as the in-plane toroidal dipole does. With regard to modes IV or VI, the circular electric field generated in the x-z or y-z planes demonstrates the magnetic dipole moment oscillation along the y or x axis as shown in Figs. 3(d), 3(f), S1(d), S1(f), and S2(d)–S2(f).

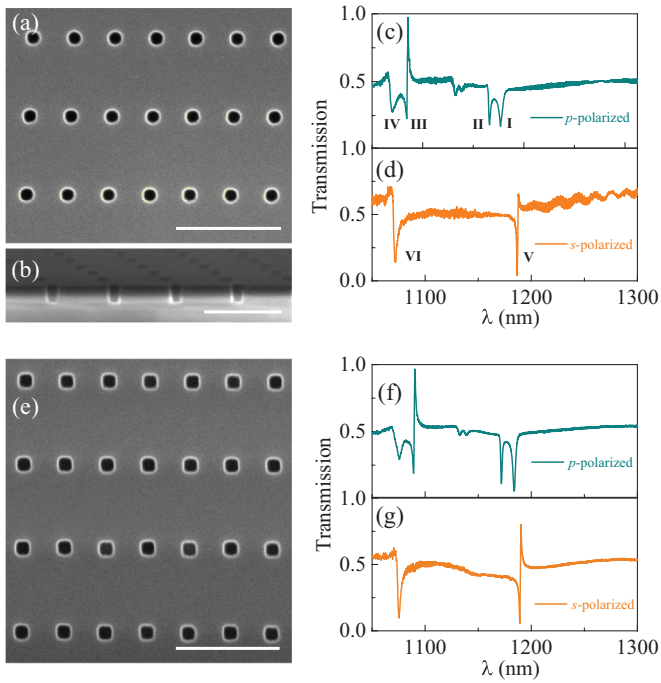

FIG. 4. (a), (b), (e) The SEM images of circular and square hole arrays. (a), (e) show the top view, and (b) shows the side view; the scale bars are 1 μm. (c), (d) The transmission spectra of circular hole arrays under excitation of p polarization and s polarization, respectively. (f), (g) The measured results of square hole arrays.

Next, we perform a series of experiments to verify the predictions of simulations. Figures 4(a), 4(b), and 4(e) show the scanning electron microscopy (SEM) images of the fabricated samples. From the Figs. 4(c) and 4(d), it can be observed that the six obvious modes I, II, . . . , VI are excited under different polarizations in the experiment. The deviations between the experiment and simulation results, such as the shapes or positions of the peaks, are induced by the fabrication imperfections such as the surface roughness and nonuniformities of nanohole arrays [56]. It is noted that there are two small dips under p polarization at wavelengths of about 1132 and 1138 nm in Fig. 4(c), while they are not obvious in the simulation [see Fig. 1(b)] due to the confinement of substantial electromagnetic power within the structure and weak coupling to the free space. In the experiment, owing to the not strictly normal incident light and fabrication imperfections, these two modes are further radiated to the free space [55]. Here, their resonance features will not be discussed further in this paper. Figures 4(f) and 4(g) are the experimental results with respect to square nanohole arrays. The same six resonance peaks are also observed.

III. CHARACTERISTICS OF RESONANCES IN THE COMPOSITE CIRCULAR AND SQUARE NANOHOLE ARRAYS

When the unit cell is composed of a circular hole and a square hole, as shown in Fig. 5(a), another mirror symmetry along the y axis is broken compared with the single nanohole cases of Figs. 1(a) and 1(d). The corresponding symmetry of

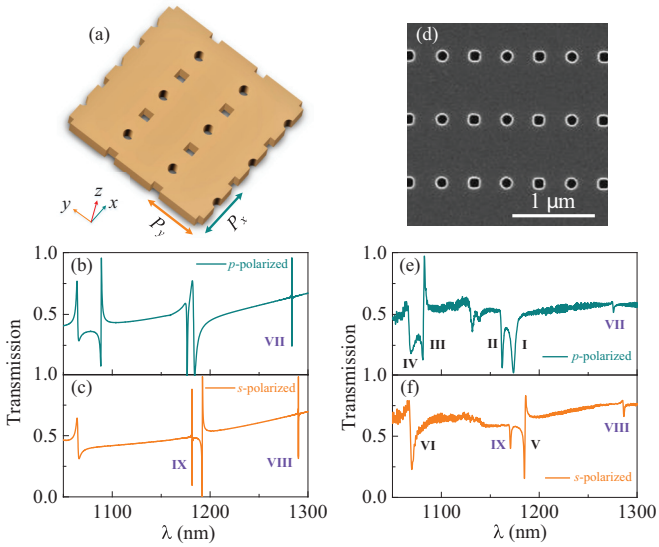

FIG. 5. (a) Schematic of the composite circular and square hole array. (d) corresponds to the SEM image of the fabricated sample. (b) and (c) are the simulated transmission spectra, and (e) and (f) are the experimental results.

the mode is broken along that axis, thus the original uncoupled mode is perturbed and the perturbed mode can be considered as a sum of a nondegenerate mode and a degenerate mode. As the degenerate part has the same symmetry with either *s*- or *p*-polarized light, the original uncoupled mode can now couple to the external radiation, and can only be excited by light with this corresponding polarization [57]. As a result, we can see three additional, much sharper Fano resonances in Figs. 5(b) and 5(c) and the zoomed resonant peaks in Fig. S3, which are denoted by VII, VIII, and IX and are missing in the independent nanohole structures of Figs. 1(a) and 1(d). Mode VII is excited by *p*-polarized light, whereas modes VIII and IX are excited by *s*-polarized light. Figure 5(d) shows the SEM image of the fabricated sample, and Figs. 5(e) and 5(f) correspond to the experimental transmission spectra, indicating that additional modes VII, VIII, and XI are also verified in the measurement. The nine Fano resonances are fitted by the classical Fano formula (see Fig. S5) [62–65]

$$T(\omega) = T_0 + A_0 \frac{[q + 2(\omega - \omega_0)/\tau]^2}{1 + [2(\omega - \omega_0)/\tau]^2}, \tag{11}$$

where ω_0 is the resonant frequency, τ is the resonance linewidth, T_0 is the transmission offset, A_0 is the continuum-discrete coupling constant, and q is the Breit-Wigner-Fano parameter determining the asymmetry of the resonance profile. The Q factor is evaluated by $\frac{\omega_0}{\tau}$. Comparing with the theoretical Q factors, the reduction of the experimental results is mainly attributed to the fabrication imperfection, which partially breaks the crystal symmetry and leads to strong scattering of light into free space [54,56].

The multipole decompositions of modes VII, VIII, and IX are shown in Figs. 6(a)–6(c). For mode VII, the toroidal moment contributes predominantly to the resonance. With regard to modes VIII and IX, the magnetic moment is dominant, with a relatively large and constant electric moment in the interesting wavelength range of mode VIII and a secondary contribution of the electric quadrupole at mode IX. The

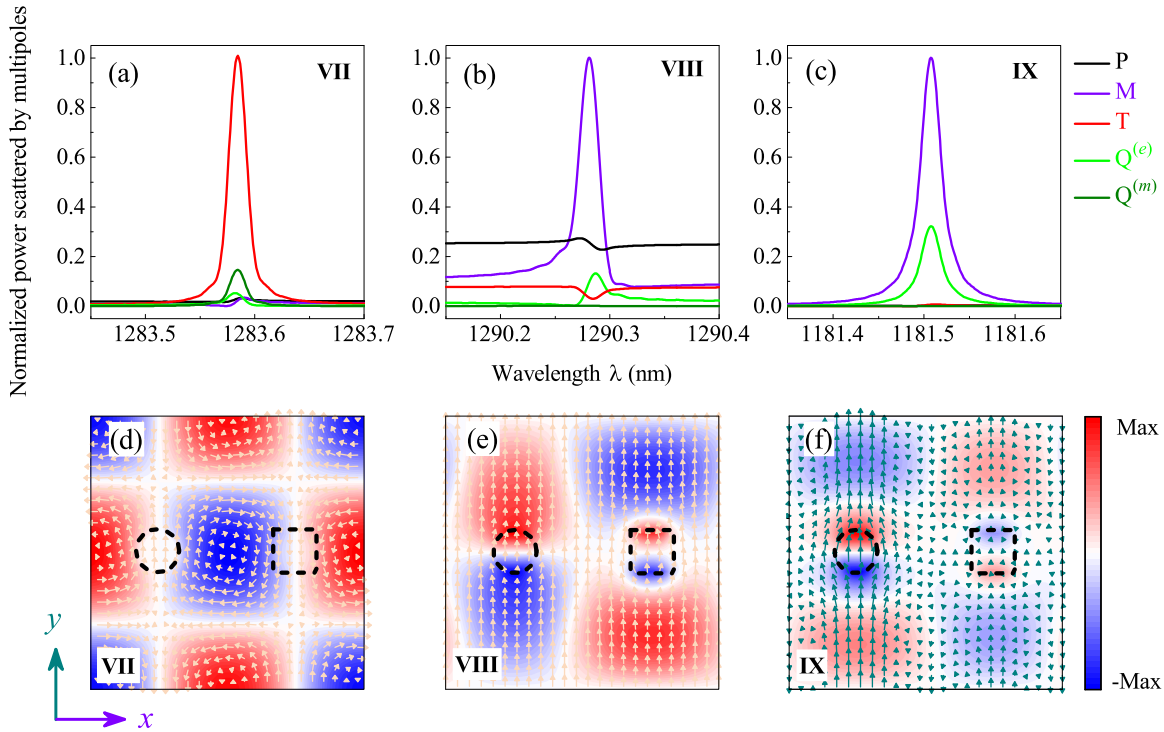

FIG. 6. (a)–(c) Normalized scattering power of the composite nanohole structure at modes VII, VIII, and IX. (d)–(f) Calculated z component of the electric field (E_z) distributions for modes VII, VIII, and IX. Arrows show instantaneous directions of the magnetic (modes VII) and electric (modes VIII and IX) field.

special electric distributions are exhibited due to introducing additional symmetry breaking, as shown in Figs. 6(d)–6(f). The field profile of the E_z components of mode VII is unchanged under the mirror reflection operation around the x axis, requiring the excitation from p-polarized light, while the field profiles of modes VIII and IX are altered by a factor of -1 under the same reflection operation and hence can be excited by s-polarized light. They are excited in our case due to the compensation of the symmetry mismatch between these modes and the incident wave through additional symmetry breaking [55,56]. Thus, the three nondegenerate modes are excited and can only couple to a single polarization with the same symmetry of these modes. Figure 6(d) corresponding to mode VII exhibits a circular magnetic field in the x-y plane, formed by a y-polarized magnetic field of incident light and an x-polarized magnetic field generated from the opposite electric field loop in the y-z plane [see Fig. S4(a)], revealing the excitation of the toroidal moment along the z axis [see Fig. S4(d)]. As for modes VIII and IX, a circular electric field gives rise to a magnetic moment oscillation along the z axis, serving as the most contributive component of the resonance. However, these electric field patterns shown in Figs. 6(e) and 6(f) fail to form an obvious loop, possibly rising from the relatively strong interference of the electric dipole or electric quadrupole for modes VIII or IX, respectively.

IV. CONCLUSIONS

In summary, by introducing symmetry breaking into a square lattice nanostructure, we have experimentally achieved multiple toroidal dipole resonances in the near-infrared range. Each dipole moment and their contributions to the far-field radiation have been discussed in depth. The near-field distributions of these resonant modes have been analyzed as well. The results indicate that there exist multiple toroidal dipole resonances in the nanohole arrays, also accompanying the excitation of the magnetic dipole resonance. It is noted that the additional toroidal dipole resonance with a higher Q factor is excited when an additional symmetry of the structure is further broken. The experimental results match well with the theoretical predictions. These two-dimensional (2D) nanohole structures with low dissipative losses would reduce nanofabrication accuracy requirements in comparison with complex 2D nanopillar structures or 3D nanostructures [30,56,58]. Therefore, our results can provide a route to achieve strong resonance with a high Q factor by taking advantage of the toroidal dipole resonance, and facilitate the development of nanophotonics in applications such as nanolasers, optical switching, biosensing, and so on.

It is noted that a toroidal dipole alone does not produce distinctive and experimentally observable effects on the transmission spectrum. However, it can be indirectly observed through the creation of a nonradiating anapole mode, produced by the destructive interference between the electric dipole and toroidal dipole. When their moments satisfy $\vec{P} = -ik\vec{T}$, their radiation fields interfere destructively owing to the similarity of their far-field scattering patterns [24,28]. An anapole mode can manifest itself in the extinction spectrum as a dip and produce a significant enhancement in the near field around the structure which can be measured by a near-field scanning optical microscope. Owing to the strong confinement of energy, nanostructures supporting anapoles have been applied in harmonic generation [14,66,67], Raman scattering enhancement [68], nanolasers [69], and so on.

ACKNOWLEDGMENTS

The authors thank all the engineers in the Center of Micro Fabrication and Characterization (CMFC) of Wuhan National Laboratory for Optoelectronics (WNLO) for their support in fabrication. This work was supported by the National Natural Science Foundation of China (Grant No. 61775075).

APPENDIX

Sample fabrication. The samples are fabricated on silicon-on-insulator (SOI) wafers with 220-nm silicon on the top layer and a 2-μm buried oxide layer. The fabrication processes mainly include electron-beam lithography (EBL) and inductively coupled plasma (ICP) etching techniques. For a start, a clean SOI flake is spin coated with 340-nm ZEP-520A as a resist layer. Then the nanohole array patterns are defined into the resist by the EBL (Vistec EBPG 5000 Plus) tool, where the beam current is about 0.5 nA, the exposure dose is 220 μC/cm^2, and the beam step size is 4 nm. After being carefully developed and fixed, the patterns are transferred to the silicon diaphragm by the ICP reactive-ion etching (ICP-RIE) (Oxford Plasmalab System 100 ICP180) technique using a SF_6/C_4F_8 mixture. The remaining resist is ultrasonically removed by dipping into the N-methyl-2-pyrrolidone (NMP) liquor. The fabricated structures are shown in Figs. 4(a), 4(b), 4(e), and 5(d).

Transmission measurements. We measure these fabricated samples with a home-built setup, with a broadband picosecond pulsing laser (YSL Photonics SC-5-FC) that covers the wavelength range from 480 to 2200 nm. The light is focused onto a spot with $1/e^2$ intensity and a diameter of $\sim$200 μm, and is launched on the sample at normal incidence. The size of the fabricated sample is large enough (560 μm $\times$ 560 μm) to ensure that the whole light beam passes through the patterned area. The light transmitted by the sample is collected by an optical spectrometer (Yokogawa AQ-6370). It is noted that the light first passes through a linear polarizer, so that only a single polarization is used to study the polarization characteristics of these resonance modes. Transmittance through the sample is referenced to the transmittance through the unpatterned area.

Electromagnetic simulations. The optical responses of nanohole structures are calculated by the finite-difference time-domain (FDTD) method. In the simulation, the periodical boundary conditions are used along the x and y directions, and perfectly matched layers are used in the z direction. The complex dielectric constants of silicon and silica are taken from Palik [70].

[1] K. Tanaka, E. Plum, J. Y. Ou, T. Uchino, and N. I. Zheludev, Phys. Rev. Lett. **105**, 227403 (2010).

[2] I. Staude, V. V. Khardikov, N. T. Fofang, S. Liu, M. Decker, D. N. Neshev, T. S. Luk, I. Brener, and Y. S. Kivshar, ACS Photonics **2**, 172 (2015).

[3] J. Bohn, T. Bucher, K. E. Chong, A. Komar, D.-Y. Choi, D. N. Neshev, Y. S. Kivshar, T. Pertsch, and I. Staude, Nano Lett. **18**, 3461 (2018).

[4] C. Cui, C. Zhou, S. Yuan, X. Qiu, L. Zhu, Y. Wang, Y. Li, J. Song, Q. Huang, Y. Wang *et al.*, ACS Photonics **5**, 4074 (2018).

[5] S. Liu, A. Vaskin, S. Addamane, B. Leung, M.-C. Tsai, Y. Yang, P. P. Vabishchevich, G. A. Keeler, G. Wang, X. He *et al.*, Nano Lett. **18**, 6906 (2018).

[6] C. Wu, A. B. Khanikaev, R. Adato, N. Arju, A. A. Yanik, H. Altug, and G. Shvets, Nat. Mater. **11**, 69 (2012).

[7] A. Farmani, A. Mir, M. Bazgir, and F. B. Zarrabi, Physica E **104**, 233 (2018).

[8] K. V. Sreekanth, S. Sreejith, S. Han, A. Mishra, X. Chen, H. Sun, C. T. Lim, and R. Singh, Nat. Commun. **9**, 369 (2018).

[9] M. R. Shcherbakov, P. P. Vabishchevich, A. S. Shorokhov, K. E. Chong, D.-Y. Choi, I. Staude, A. E. Miroshnichenko, D. N. Neshev, A. A. Fedyanin, and Y. S. Kivshar, Nano Lett. **15**, 6985 (2015).

[10] A. Komar, R. Paniagua-Dominguez, A. Miroshnichenko, Y. F. Yu, Y. S. Kivshar, A. I. Kuznetsov, and D. Neshev, ACS Photonics **5**, 1742 (2018).

[11] M. R. Shcherbakov, D. N. Neshev, B. Hopkins, A. S. Shorokhov, I. Staude, E. V. Melik-Gaykazyan, M. Decker, A. A. Ezhov, A. E. Miroshnichenko, I. Brener *et al.*, Nano Lett. **14**, 6488 (2014).

[12] W. Tong, C. Gong, X. Liu, S. Yuan, Q. Huang, J. Xia, and Y. Wang, Opt. Express **24**, 19661 (2016).

[13] Y. Liu, S. Wang, D. Zhao, W. Zhou, and Y. Sun, Opt. Express **25**, 10536 (2017).

[14] L. Xu, M. Rahmani, K. Z. Kamali, A. Lamprianidis, L. Ghirardini, J. Sautter, R. Camacho-Morales, H. Chen, M. Parry, I. Staude, G. Zhang, D. Neshev, and A. E. Miroshnichenko, Light: Sci. Appl. **7**, 44 (2018).

[15] C. Zhou, C. Gong, G. Ban, S. Li, Y. Wang, X. Liu, and M. Zhan, in *POEM Optoelectronic Devices and Integration* (Optical Society of America, Washington, DC, 2018), pp. OT4A–32.

[16] H. Liu, C. Guo, G. Vampa, J. L. Zhang, T. Sarmiento, M. Xiao, P. H. Bucksbaum, J. Vučković, S. Fan, and D. A. Reis, Nat. Phys. **14**, 1006 (2018).

[17] I. B. Zel'Dovich, J. Exptl. Theor. Phys. (U.S.S.R.) **33**, 1488 (1957) [Sov. Phys. JETP **6**, 1188 (1958)].

[18] N. Papasimakis, V. Fedotov, V. Savinov, T. Raybould, and N. Zheludev, Nat. Mater. **15**, 263 (2016).

[19] T. Kaelberer, V. Fedotov, N. Papasimakis, D. Tsai, and N. Zheludev, Science **330**, 1510 (2010).

[20] A. Ahmadivand, B. Gerislioglu, P. Manickam, A. Kaushik, S. Bhansali, M. Nair, and N. Pala, ACS Sens. **2**, 1359 (2017).

[21] M. Gupta, Y. K. Srivastava, M. Manjappa, and R. Singh, Appl. Phys. Lett. **110**, 121108 (2017).

[22] G.-D. Liu, X. Zhai, S.-X. Xia, Q. Lin, C.-J. Zhao, and L.-L. Wang, Opt. Express **25**, 26045 (2017).

[23] B. Gerislioglu, A. Ahmadivand, and N. Pala, Phys. Rev. B **97**, 161405(R) (2018).

[24] A. E. Miroshnichenko, A. B. Evlyukhin, Y. F. Yu, R. M. Bakker, A. Chipouline, A. I. Kuznetsov, B. Luk'yanchuk, B. N. Chichkov, and Y. S. Kivshar, Nat. Commun. **6**, 8069 (2015).

[25] L. Wei, Z. Xi, N. Bhattacharya, and H. P. Urbach, Optica **3**, 799 (2016).

[26] A. A. Basharin, V. Chuguevsky, N. Volsky, M. Kafesaki, and E. N. Economou, Phys. Rev. B **95**, 035104 (2017).

[27] Y. Yang and S. I. Bozhevolnyi, Nanotechnology **30**, 204001 (2019).

[28] P. C. Wu, C. Y. Liao, V. Savinov, T. L. Chung, W. T. Chen, Y.-W. Huang, P. R. Wu, Y.-H. Chen, A.-Q. Liu, N. I. Zheludev, and D. P. Tsai, ACS Nano **12**, 1920 (2018).

[29] S.-D. Liu, J.-L. Fan, W.-J. Wang, J.-D. Chen, and Z.-H. Chen, ACS Photonics **5**, 1628 (2018).

[30] A. K. Ospanova, I. V. Stenishchev, and A. A. Basharin, Laser Photonics Rev. **12**, 1800005 (2018).

[31] Y.-W. Huang, W. T. Chen, P. C. Wu, V. Fedotov, V. Savinov, Y. Z. Ho, Y.-F. Chau, N. I. Zheludev, and D. P. Tsai, Opt. Express **20**, 1760 (2012).

[32] Z.-G. Dong, J. Zhu, J. Rho, J.-Q. Li, C. Lu, X. Yin, and X. Zhang, Appl. Phys. Lett. **101**, 144105 (2012).

[33] Z.-G. Dong, P. Ni, J. Zhu, X. Yin, and X. Zhang, Opt. Express **20**, 13065 (2012).

[34] Y. Fan, Z. Wei, H. Li, H. Chen, and C. M. Soukoulis, Phys. Rev. B **87**, 115417 (2013).

[35] M. Gupta and R. Singh, Adv. Opt. Mater. **4**, 2119 (2016).

[36] V. R. Tuz, V. V. Khardikov, A. S. Kupriianov, K. L. Domina, S. Xu, H. Wang, and H.-B. Sun, Opt. Express **26**, 2905 (2018).

[37] J. B. Khurgin, Nat. Nanotechnol. **10**, 2 (2015).

[38] A. I. Kuznetsov, A. E. Miroshnichenko, M. L. Brongersma, Y. S. Kivshar, and B. Luk'yanchuk, Science **354**, aag2472 (2016).

[39] I. Staude, A. E. Miroshnichenko, M. Decker, N. T. Fofang, S. Liu, E. Gonzales, J. Dominguez, T. S. Luk, D. N. Neshev, I. Brener *et al.*, ACS Nano **7**, 7824 (2013).

[40] J. Zhang, K. F. MacDonald, and N. I. Zheludev, Opt. Express **21**, 26721 (2013).

[41] L. Huang, Y. Yu, and L. Cao, Nano Lett. **13**, 3559 (2013).

[42] K. E. Chong, B. Hopkins, I. Staude, A. E. Miroshnichenko, J. Dominguez, M. Decker, D. N. Neshev, I. Brener, and Y. S. Kivshar, Small **10**, 1985 (2014).

[43] B. Hopkins, D. S. Filonov, A. E. Miroshnichenko, F. Monticone, A. Aluù, and Y. S. Kivshar, ACS Photonics **2**, 724 (2015).

[44] M. Decker, I. Staude, M. Falkner, J. Dominguez, D. N. Neshev, I. Brener, T. Pertsch, and Y. S. Kivshar, Adv. Opt. Mater. **3**, 813 (2015).

[45] I. Staude and J. Schilling, Nat. Photonics **11**, 274 (2017).

[46] C. Zhang, Y. Xu, J. Liu, J. Li, J. Xiang, H. Li, J. Li, Q. Dai, S. Lan, and A. E. Miroshnichenko, Nat. Commun. **9**, 2964 (2018).

[47] P. Yu, A. S. Kupriianov, V. Dmitriev, and V. R. Tuz, J. Appl. Phys. **125**, 143101 (2019).

[48] A. Sayanskiy, A. S. Kupriianov, S. Xu, P. Kapitanova, V. Dmitriev, V. V. Khardikov, and V. R. Tuz, Phys. Rev. B **99**, 085306 (2019).

[49] A. A. Basharin, M. Kafesaki, E. N. Economou, C. M. Soukoulis, V. A. Fedotov, V. Savinov, and N. I. Zheludev, Phys. Rev. X **5**, 011036 (2015).

[50] A. Sayanskiy, M. Danaeifar, P. Kapitanova, and A. E. Miroshnichenko, Adv. Opt. Mater. **6**, 1800302 (2018).

[51] S. Xu, A. Sayanskiy, A. S. Kupriianov, V. R. Tuz, P. Kapitanova, H.-B. Sun, W. Han, and Y. S. Kivshar, Adv. Opt. Mater. **7**, 1801166 (2019).
[52] V. R. Tuz, V. V. Khardikov, and Y. S. Kivshar, ACS Photonics **5**, 1871 (2018).
[53] S. Fan and J. D. Joannopoulos, Phys. Rev. B **65**, 235112 (2002).
[54] C. Zhou, G. Liu, G. Ban, S. Li, Q. Huang, J. Xia, Y. Wang, and M. Zhan, Appl. Phys. Lett. **112**, 101904 (2018).
[55] K. B. Crozier, V. Lousse, O. Kilic, S. Kim, S. Fan, and O. Solgaard, Phys. Rev. B **73**, 115126 (2006).
[56] J. Lee, B. Zhen, S.-L. Chua, W. Qiu, J. D. Joannopoulos, M. Soljačić, and O. Shapira, Phys. Rev. Lett. **109**, 067401 (2012).
[57] O. Kilic, M. Digonnet, G. Kino, and O. Solgaard, Opt. Express **16**, 13090 (2008).
[58] C. Nicolaou, W. T. Lau, R. Gad, H. Akhavan, R. Schilling, and O. Levi, Opt. Express **21**, 31698 (2013).
[59] C. W. Hsu, B. Zhen, J. Lee, S.-L. Chua, S. G. Johnson, J. D. Joannopoulos, and M. Soljačić, Nature (London) **499**, 188 (2013).
[60] M. Gupta, V. Savinov, N. Xu, L. Cong, G. Dayal, S. Wang, W. Zhang, N. I. Zheludev, and R. Singh, Adv. Mater. **28**, 8206 (2016).
[61] See Supplemental Material at http://link.aps.org/supplemental/10.1103/PhysRevB.100.195306 for the electric and magnetic field distributions in the *x*-*z* or *y*-*z* planes for modes I–VI, the power scattered by components of toroidal dipole or magnetic dipole for modes I–VI, the detailed transmission spectra for modes VII–IX, the electric and magnetic field distributions in the *x*-*z* or *y*-*z* planes and power scattered by multipole components of toroidal dipole or magnetic dipole for modes VII, VIII, and IX, and the Fano fitting of the nine modes in the composite circular and square hole arrays .
[62] M. Galli, S. Portalupi, M. Belotti, L. Andreani, L. O'Faolain, and T. Krauss, Appl. Phys. Lett. **94**, 071101 (2009).
[63] A. E. Miroshnichenko, S. Flach, and Y. S. Kivshar, Rev. Mod. Phys. **82**, 2257 (2010).
[64] A. A. Yanik, A. E. Cetin, M. Huang, A. Artar, S. H. Mousavi, A. Khanikaev, J. H. Connor, G. Shvets, and H. Altug, Proc. Natl. Acad. Sci. USA **108**, 11784 (2011).
[65] W. X. Lim, M. Manjappa, P. Pitchappa, and R. Singh, Adv. Opt. Mater. **6**, 1800502 (2018).
[66] T. Shibanuma, G. Grinblat, P. Albella, and S. A. Maier, Nano Lett. **17**, 2647 (2017).
[67] G. Grinblat, Y. Li, M. P. Nielsen, R. F. Oulton, and S. A. Maier, ACS Nano **11**, 953 (2016).
[68] D. G. Baranov, R. Verre, P. Karpinski, and M. Kall, ACS Photonics **5**, 2730 (2018).
[69] J. S. T. Gongora, A. E. Miroshnichenko, Y. S. Kivshar, and A. Fratalocchi, Nat. Commun. **8**, 15535 (2017).
[70] E. D. Palik, *Handbook of Optical Constants of Solids*, Vol. 3 (Academic, New York, 1998).